Fiber-based ultrashort pulse delivery for nonlinear imaging using high-energy solitons

Sarah Saint-Jalm
Esben R. Andresen
Patrick Ferrand
Abdelkrim Bendahmane
Arnaud Mussot
Olivier Vanvincq
Géraud Bouwmans
Alexandre Kudlinski
Hervé Rigneault

SPIE.

Fiber-based ultrashort pulse delivery for nonlinear imaging using high-energy solitons

Sarah Saint-Jalm,[a] Esben R. Andresen,[a] Patrick Ferrand,[a] Abdelkrim Bendahmane,[b] Arnaud Mussot,[b] Olivier Vanvincq,[b] Géraud Bouwmans,[b] Alexandre Kudlinski,[b] and Hervé Rigneault[a,*]
[a]Aix Marseille Université, CNRS, Centrale Marseille, Institut Fresnel, UMR 7249, Faculté des Sciences Saint-Jérôme, 13013 Marseille, France
[b]Université Lille 1, IRCICA, Laboratoire PhLAM, 59655 Villeneuve d'Ascq, France

Abstract. We present an approach for fiber delivery of femtosecond pulses relying on pulse breakup and soliton self-frequency shift in a custom-made solid-core photonic bandgap fiber. In this scheme, the fiber properties themselves ensure that a powerful Fourier-transform-limited pulse is emitted at the fiber output, hence doing away with the need for complex precompensation and enabling tunability of the excitation. We report high-energy soliton excitation for two-photon fluorescence microspectroscopy over a 100-nm range and multimodal nonlinear imaging on biological samples. © *2014 Society of Photo-Optical Instrumentation Engineers (SPIE)* [DOI: 10.1117/1.JBO.19.8.086021]

1 Introduction

The growing interest in point-scanning microscopy techniques based on nonlinear contrasts such as multiphoton excitation fluorescence, second-harmonic generation (SHG), and third-harmonic generation or coherent Raman scattering[1,2] has lead to an increasing need for powerful and versatile light sources. Such a source must generate near-infrared (NIR) ultrashort pulses (typically $\approx$100 fs) with peak powers high enough to observe signals generated by nonlinear processes taking place in the focal volume. Most of the nonlinear microscopes use bulky optics to relay ultrashort pulses between the femtosecond laser and the microscope stand. Many applications would benefit from fiber delivery of high-energy femtosecond pulses. Such systems would also be very beneficial to the emerging field of local probe or endoscopic nonlinear imaging that aims at miniaturizing point-scanning techniques for sensor and biomedical applications. Although several successful experiments have been conducted over the past 10 years, fiber delivery of Fourier-transform-limited femtosecond pulses remains a challenge today. Various strategies have been explored to address this issue, most of them using Ti:Sapphire lasers for pulse generation in the NIR (800 to 1000 nm) and a variety of fibers for pulse propagation and delivery, such as single-mode fibers,[3] double-clad fibers,[4,5] fiber bundles,[6] large-mode area fibers,[7] double-clad photonic crystal fibers (PCFs),[8,9] and hollow-core photonic bandgap fibers.[10–13] Recently, Er- and Yb-doped fiber lasers have been put to use in a new type of all-fiber-optic endoscopes operating at >1-μm wavelength.[14,15] In most of those examples, the dispersion and nonlinearities of the delivering fibers distort and temporally broaden the pulse. Simultaneous precompensation for dispersion and nonlinearity is complex[16,17] and only gives a transform-limited output pulse within a narrow input parameter range. Furthermore, none of those techniques allow rapid wavelength tuning of the delivered pulse.

An alternative approach consists of taking advantage of the nonlinearities of a PCF in the anomalous dispersion regime. In this case, fundamental solitons are ejected and red-shifted after pulse breakup and the subsequent soliton self-frequency shift (SSFS).[18] This way, a femtosecond pulse is generated and delivered by the same fiber. Only fundamental solitons are stable in optical fibers, so the pulse is intrinsically Fourier-transform-limited at the output of the fiber due to the balance between anomalous dispersion and the Kerr nonlinearity responsible for soliton dynamics. Increasing the power at the input of the fiber results in a greater soliton redshift, which opens the door to spectroscopic applications and hyperspectral imaging. This is an elegant way of solving the precompensation problem while enabling tunability.[19] Solitons of >1-μm wavelengths have been previously used to perform multiphoton microscopy.[20–22] In this paper, we present results obtained with a custom-made solid-core photonic bandgap (SC-PBG) fiber that has been designed for generating powerful solitons from 800 to 1000 nm, an ideal range for performing microscopy on biological samples. In contrast to previous works in which generation of high-energy solitons in hollow-core photonic bandgap fibers[23] and higher-order-mode fibers[24] have been reported, we propose an approach that allows the generation of powerful solitons at input powers compatible with standard light sources available in microscopy labs. We characterize the fiber, demonstrate its use in a spectroscopic scheme, and illustrate its ability to generate two-photon excitation fluorescence (TPEF) and SHG images of biological samples.

2 Methods

2.1 Soliton Dynamics

The propagation of light in a PCF along its main axis z is governed by the nonlinear Schrödinger equation (NLSE)[25]

*Address all correspondence to: Hervé Rigneault, E-mail: herve.rigneault@fresnel.fr

$$\frac{\partial E(z,t)}{\partial z} = -\frac{i}{2}\beta_2 \frac{\partial^2 E(z,t)}{\partial t^2} + i\gamma |E(z,t)|^2 E(z,t), \tag{1}$$

where β_2 is the group velocity dispersion (GVD) and γ is the nonlinear parameter. Those two wavelength-dependent parameters characterize the PCF and can be changed only by modifying its design.

An analytical solution to the NLSE can be found in the case of anomalous dispersion ($\beta_2 < 0$). This solution describes a pulse of light that propagates without changing its shape, known as a fundamental soliton. It can be expressed as follows:

$$E(z,t) = \sqrt{P_0} \cdot \text{sech}\left(\frac{t}{T_0}\right) \cdot \exp\left(\frac{i|\beta_2|z}{T_0^2}\right), \tag{2}$$

where P_0 is the peak power of the soliton and T_0 is its duration, defined with respect to the full width at half maximum duration by $T_{\text{FWHM}} = 2\ln(1+\sqrt{2})T_0$. Soliton dynamics relies on the interplay between the two processes involved in Eq. (1): the anomalous GVD (β_2) and the self-phase modulation created by the nonlinear Kerr effect (γ) act against each other in a balanced way, which ensures the preservation of the pulse shape. This relationship is summed up in the following equation, which also links the power and duration of the solitons to each other and to the fiber parameters

$$N^2 = \frac{\gamma P_0 T_0^2}{|\beta_2|}, \tag{3}$$

where N is the soliton order. In this paper, we are only generating fundamental solitons, for which $N = 1$, because higher-order solitons are not stable in optical fibers due to their intrinsic higher-order dispersion and/or Raman nonlinearity.

For short pulses (<5 ps), the simplest form of the NLSE [Eq. (1)] is not sufficient to fully describe the behavior of solitons. Higher-order effects have to be taken into account, particularly intrapulse Raman scattering, which is responsible for the SSFS that we will use as a tuning mechanism. When the pulse is very short (typically $\approx$100 fs), its spectrum is broad enough that an effect similar to stimulated Raman scattering can occur between the blue and the red components, mediated by the vibration modes of silica. Namely, the red part of the spectrum experiences a Raman gain, while the blue part experiences a Raman loss. This results in the continuous redshift of the soliton along its propagation in the fiber. The variation of the central frequency of the soliton is related to the duration of the pulse

$$\Delta\omega_R \propto -\frac{|\beta_2|z}{T_0^4}. \tag{4}$$

When more power is injected into the fiber, the duration of the pulse decreases [see Eq. (3)], therefore, the redshift is enhanced. We propose to use this effect as a wavelength tuning mechanism. Indeed, since the redshift is proportional to T_0^{-4}, a small variation in the pulse duration will cause a large redshift and we can obtain a large tuning range for a virtually constant T_0.

If the third-order dispersion is small enough, the shape of the pulse remains the same during propagation and it is Fourier-transform-limited at any z in the fiber, which means that it is the shortest pulse allowed by its bandwidth, with a constant time-bandwidth product $\Delta t_{\text{FWHM}} \Delta\nu_{\text{FWHM}} = 4[\ln(1+\sqrt{2})]^2/\pi^2 \approx 0.315$ characteristic for sech^2 pulses. This is an interesting property for nonlinear microscopy as the contrasts we wish to activate require a high peak power, and therefore a short pulse duration.

2.2 SC-PBG Fiber

From Eq. (3), we get that the energy of the soliton depends on the dispersion to nonlinear coefficient ratio ($|\beta_2|/\gamma$) which are the parameters of the fiber. We can rewrite it in the following way:

$$E_{\text{sol}} = \frac{2|\beta_2|}{T_0\gamma}. \tag{5}$$

In order to get high excitation powers compatible with nonlinear microscopy, one has to fabricate a fiber whose design provides a high $|\beta_2|/\gamma$ ratio. We designed and fabricated an SC-PBG fiber with a doubly periodic cladding consisting of high index inclusions made of germanium-doped silica that are responsible for photonic bandgap guidance and air holes for reducing the confinement losses. Figure 1(a) shows a scanning electron microscope image of the fiber. This fiber resembled the one in Ref. 26, although the transmission window was optimized for 800 nm lasers. In the present SC-PBG fiber, the generation and redshift of solitons are possible in the first PBG, from the zero dispersion wavelength at 750 nm to the long-wavelength edge at 1030 nm. Such a fiber was shown to generate 3 to 5 times higher-energy solitons than standard PCFs.[27] Figure 1(b) shows the $|\beta_2|/\gamma$ ratio for the fiber we used in comparison to standard values for other PCFs. Coupling efficiencies were about 30% to 40% and the soliton generation efficiency, defined as the ratio of the soliton power over the total input power, was about 10%.

2.3 Optical Setups

2.3.1 Characterization of the SC-PBG fiber

We launched NIR femtosecond pulses (800 nm, 30 fs, 1 GHz) in sections of the fiber of various lengths for characterization at different input powers. The light was coupled into the fiber with an aspheric lens. To get coupling to the fundamental mode, we imaged the exit end of the fiber on a CMOS camera and maximized the intensity of this mode. The input power was controlled by a half-wave plate and a polarizing beam splitter. The resulting solitons were filtered from the residue of the laser light at 800 nm as well as the blue-shifted dispersive waves by long-pass filters (LP830RU from Semrock, Rochester, New York or FEL850 from Thorlabs, Newton, New Jersey), and some of their properties were measured, such as average power, spectrum (USB2000, Ocean Optics, Dunedin, Florida), and duration through their autocorrelation trace (Mini, APE, Berlin, Germany).

2.3.2 Spectroscopy and microscopy

We conducted two sets of experiments based on the excitation of the sample by the optical solitons generated in the fiber. First, we performed microspectroscopy on liquid samples, then we did microscopy on several samples, including biological ones.

The solitons were generated by a coupling 800 nm light from either an 80 MHz (Chameleon, 150 fs from Coherent Inc., Santa
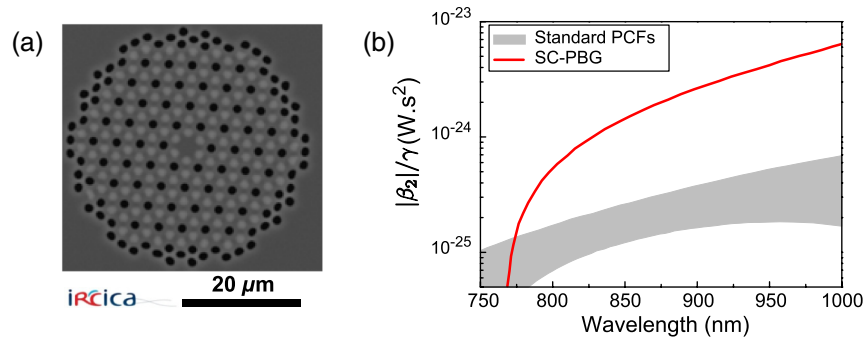
Fig. 1 (a) Scanning electron microscope image of the solid-core photonic bandgap (SC-PBG) fiber. Dark gray: silica; light gray: Ge-doped silica; black: air. (b) Red line: $|\beta_2|/\gamma$ ratios calculated for the SC-PBG fiber used in this work (finite element method simulation). Gray area: typical values of this ratio for standard PCFs.

Clara, California) or a 1 GHz laser (GigaJet, 30 fs from Laser Quantum, Stockport, United Kingdom) into the SC-PBG fiber. As before, the soliton wavelength was controlled by changing the input power, and was filtered from residual and dispersive waves with a long-pass filter to ensure that the soliton was the only excitation pulse reaching the sample. For microspectroscopy, the light was focused on the sample with a long working distance objective (20×, NA = 0.45 from Olympus, Tokyo, Japan) and collected by another objective (NA = 0.60) in the forward direction. We detected the TPEF on an APD after a set of long-pass and bandpass filters.

For microscopy, we used a high NA objective (40×, NA = 1.15, water immersion from Nikon, Tokyo, Japan) and scanned the focus across the sample with galvanometric mirrors to create TPEF and SHG images in an epi-detection scheme by using two PMTs and an appropriate set of filters and dichroic mirrors.

A scheme representing the two setups combined is shown in Fig. 2.

3 Results and Discussion

3.1 Generation of Solitons in the SC-PBG Fiber

An example of output spectrum is shown in Fig. 3(a). The red-shifted soliton is perfectly fitted by a squared hyperbolic-secant function (red dotted line). The inset of Fig. 3(a) shows the
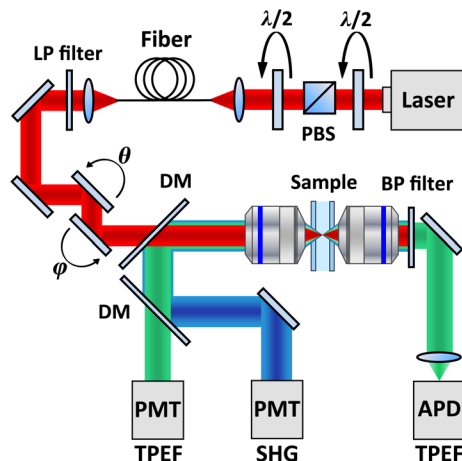
Fig. 2 Scheme of the microspectroscopy and microscopy setup. PBS: polarizing beam splitter; $\lambda/2$: half-wave plate; DM: dichroic mirror; LP/BP filter: long-pass/bandpass filter; PMT: photomultiplier tube; and APD: avalanche photodiode.

autocorrelation trace for the 900 nm soliton corresponding to the spectrum. For sech^2 pulses, we divide the width FWHM of the autocorrelation trace by 1.54 in order to recover the pulse duration, which in this case was found to be 90 fs. The Fourier-transform-limited duration calculated from the Fourier transform of the spectrum ($\Delta\lambda = 10.7$ nm) is 80 fs. The difference can be explained by the dispersion of the optics between the fiber and the autocorrelator (lens, filter, halfwave plate), estimated to be about 1200 fs^2. Thus we verify that the soliton is Fourier-transform-limited at the output of the fiber.

Figure 3(b) shows the measured energy of the solitons through the whole tunability window. For each measured point in Fig. 3(b), we calculate the effective $|\beta_2|/\gamma$ ratio with Eq. (3), using duration values calculated from the Fourier transform of the measured spectrum. Figure 3(c) shows those experimental values along with the theoretical curve from finite element method calculations.

We find a good agreement between the simulation and the experiment for fibers up to 10 m, whereas in longer fibers, the calculated $|\beta_2|/\gamma$ ratios are lower than the theory. In a similar fashion, the highest redshift accessible via SSFS increases with fiber length, but it reaches a maximum value at $L = 10$ m [see Fig. 3(d)].

In fibers longer than 15 m, several mechanisms can explain the lower values of the effective $|\beta_2|/\gamma$ and the end of the red-shift. First, the third-order dispersion arising when the soliton gets closer to the PBG edge decelerates the SSFS in the fiber.[28] Second, the attenuation experienced by the pulse when it propagates increases the nonlinear length $L_{NL} = 1/(\gamma P_0)$ which is the characteristic length needed for the soliton to adapt to any changes. At a certain point, the soliton can no longer follow the changes in P_0, ceases to redshift, and temporally broadens under dispersion. In the end, the redshifted pulse loses its soliton nature during propagation, and Eq. (3) is no longer valid. Figure 3(d) can be interpreted as the redshift versus the fiber length. In view of the above explanation, we can say that soliton nature of the pulse is retained until the plateau.

Finally, we achieve a 100 nm tuning range for the soliton. The length of the fiber must be less than 10 m so that Eq. (3) is still valid and the output pulse is Fourier-transform-limited. Then, the fiber length should be chosen according to the tunability and power requirements for the application. In the experiments described in the following, we used the 10-m fiber for spectroscopic application because it displays the best trade-off between tunability and soliton power, and the 3-m fiber for microscopy to get high soliton power.
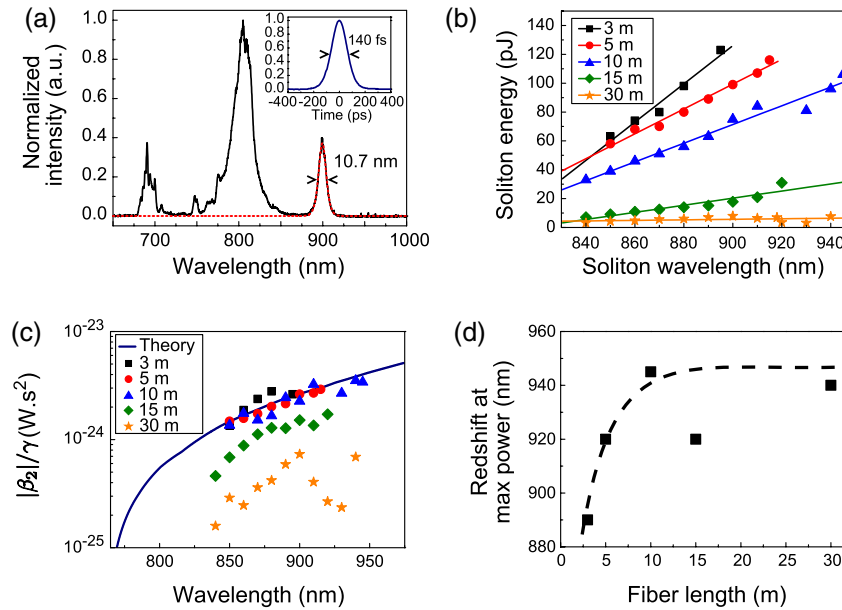
Fig. 3 (a) Black line: spectrum of the output of the fiber. Red dotted line: squared hyperbolic-secant fit of the soliton. Inset: autocorrelation trace of the 900 nm soliton. (b) Wavelength dependence of the energy of the soliton for fiber lengths from 3 to 30 m. The full lines are linear fits of the experimental points for each fiber. Fiber input average powers were (at 1 GHz): 420 to 1400 mW (3 m); 420 to 1360 mW (5 m); 200 to 1380 mW (10 m); 250 to 1300 mW (15 m); 200 to 1400 mW (30 m). (c) Theoretical $|\beta_2|/\gamma$ ratio (blue line) from simulation and experimental values of this ratio retrieved from measurement of the power and spectrum of the solitons, for several fiber lengths and soliton wavelengths. (d) Redshift of the soliton at maximum input power for varying fiber lengths. The dashed line is a guide to the eye.

3.2 Microspectroscopy

We investigated the TPEF response of an aqueous solution of rhodamine 6G with the setup described above. We first compared the fluorescent levels and the signal-to-noise ratios in the cases of the excitation by solitons generated in the fiber at 80 MHz and at 1 GHz.

The TPEF signal at a given wavelength depends on pulse power, duration, and repetition rate f_{rep} in the following way:[29]

$$\langle F \rangle \propto \frac{P_{av}^2}{f_{rep} \cdot T_0} = 4P_0^2 \cdot T_0 \cdot f_{rep}, \qquad (6)$$

where P_{av} is the average power and P_0 is the peak power. The energy and duration of one soliton at a given wavelength are fixed by the fiber parameters. Consequently, the only way to significantly increase the TPEF signal in this scheme is to increase the repetition rate.

More specifically, we expect the fluorescence signal to scale linearly with the repetition rate. If the TPEF photon count $S_{1\,sol}$ arising from excitation with a single soliton has mean $\langle S_{1\,sol} \rangle$ and standard deviation $\sigma_{1\,sol}$, then it follows from the properties of the standard deviation that the TPEF count rate arising from a train of solitons at repetition rate f_{rep} has mean $\langle S \rangle \propto f_{rep} \langle S_{1\,sol} \rangle$ and standard deviation $\sigma \propto \sqrt{f_{rep}} \sigma_{1\,sol}$. We can then expect both the noise and the signal-to-noise ratio to scale with the square root of the repetition rate.

We measure a 10-fold increase of the fluorescence counts and a 4-fold increase of the signal-to-noise ratio under a 12.5-fold increase of the repetition rate (from 80 MHz to 1 GHz), as shown in the inset of Fig. 4. The experimental data seem to generally follow the trend predicted by the above

calculation. This indicates that we observe only limited saturation effects in the sample when increasing the repetition rate.

The main plot in Fig. 4 shows the TPEF spectra of the same rhodamine 6G solution. The two spectra (blue circles and green triangles) obtained with excitation by solitons at 80 MHz and 1 GHz were normalized with respect to their average power and repetition rate, taking into account the small saturation effect previously measured. The agreement between the two
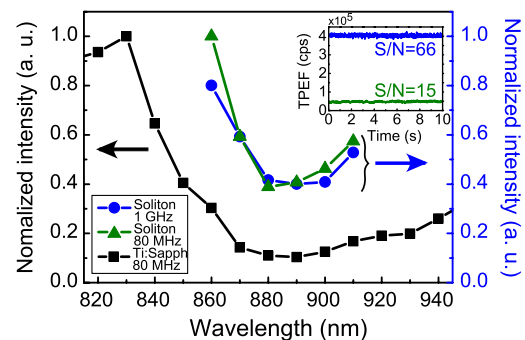
Fig. 4 Two-photon excitation fluorescence (TPEF) spectra of a 170 μM solution of rhodamine 6G in water. Black squares: reference spectrum, measured by exciting the sample with the tunable fs light directly coming from the 80 MHz Ti:Sapphire laser (without passing through the fiber). Blue circles: spectrum acquired under excitation with solitons generated in a 10 m SC-PBG fiber pumped with an 800 nm, 1 GHz laser. Green triangles: spectrum acquired under excitation with solitons generated in a 10 m SC-PBG fiber pumped with an 800 nm, 80 MHz laser. Inset: TPEF traces under excitation with 870 nm solitons at 1 GHz (blue line) and 80 MHz (green line), with the corresponding signal-to-noise ratios (in cps$^{1/2}$). Powers at the focus: black curve: 15 mW; blue: 5 mW; and green: 2 mW.
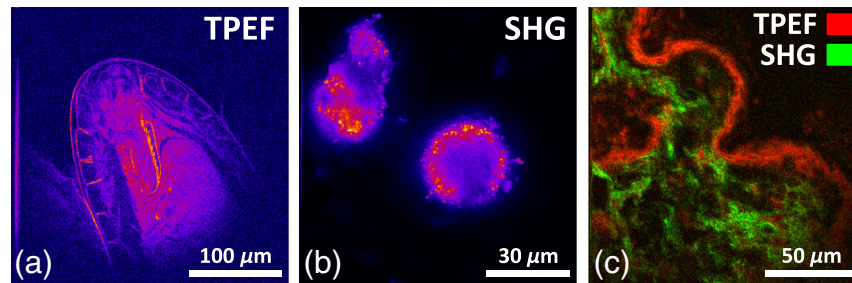
Fig. 5 300×300 pixels TPEF and second-harmonic generation (SHG) images with 10 accumulations each. (a) TPEF image of a fixed *Drosophila* embryo obtained with an 870 nm soliton excitation and a 50 μs dwell time. (b) SHG image of BaTiO$_3$ crystals obtained with an 850 nm soliton excitation and a 70 μs dwell time. (c) Composite image of fixed mouse tumor skin tissue obtained with an 870 nm soliton excitation and a 70 μs dwell time. TPEF is shown in red and SHG in green. Powers in the sample plane: (a) 40 mW; (b) 50 mW; and (c) 55 mW.

spectra is very good, proving the reliability of the soliton as a light source with only a little influence on the parameters of the pumping laser (spectrum, duration, chirp). Another spectrum was used as a control, using the fs pulse directly coming from the 80 MHz Ti:Sapphire laser (black squares) for excitation. The spectra show a good qualitative agreement. Our measurements are also consistent with the two-photon absorption cross section values for rhodamine 6G found in the literature.[29,30] However, no quantitative information can be retrieved from the comparison between this spectrum and two first spectra because many parameters vary (spectral width, pulse duration, beam shape).

3.3 Microscopy

To demonstrate the imaging capabilities of our system, we performed images of several samples, including biological ones (see Fig. 5). We generated the solitons at 1 GHz repetition rate in a 3 m fiber to operate at high excitation power and low redshift (850 to 890 nm). We first tested the two epi-detection channels separately to obtain images of samples known for their strong TPEF and SHG signals, respectively. Figure 5(a) shows a TPEF image of a fixed *Drosophila* embryo, where the formaldehyde fixation process is responsible for inducing the fluorescence signal. Figure 5(b) shows the SHG image of BaTiO$_3$ crystals. In both cases, the 50 to 70 μs dwell times that were used are comparable with the ones typically used in nonlinear microscopy. The multiphoton signal is about 10 times lower than images with standard Ti:Sapphire excitation. We have identified the reason for this discrepancy to be the spatial profile of the soliton that is singly peaked but not Gaussian. The microscope we used was not set up to compensate for this effect, which results in a bias against the soliton in this context. We then used the two channels to perform a multimodal image of a biological sample. Figure 5(c) shows a composite TPEF/SHG image of fixed mouse tumor skin tissue showing structural features that are not distinguishable in white light microscopy. The SHG emitting structures can be identified as collagen fibers, whereas TPEF comes from the stratum corneum.

4 Conclusions

We demonstrate the use in microspectroscopy and microscopy of a light source relying on soliton generation and redshift in an SC-PBG fiber. The fiber design was optimized to allow the generation of high-energy solitons, and the laws of soliton dynamics ensured a Fourier-transform-limited pulse at the exit end of the

fiber, with no need for precompensation for dispersion. For those reasons, the soliton excitation scheme is efficient for the generation of observable nonlinear signals (such as TPEF and SHG) in the focal volume. Furthermore, the power-dependent redshift of the soliton provides a 100 nm tunability range, opening the door to spectroscopic applications, hyperspectral imaging, as well as to vibrational spectroscopy and microscopy relying on coherent Raman processes. The speed of wavelength tuning is only limited by the capabilities of the devices used to change the power at the input of the fiber. For example, with a Pockels cell, one could get wavelength switching frequencies up to few MHz. In the current configuration, the wavelength tuning is repeatable enough to operate in an automated fashion over the course of a set of experiments (typically a few hours). This work emphasizes the advantages of increasing the repetition rate in terms of signal level and signal-to-noise ratio. Previous studies also suggest that photodamage associated with multiphoton excitation fluorescence decreases when the repetition rate increases while keeping a constant signal rate,[31] which is another point in favor of our 1 GHz system for soliton imaging applications of biological samples.

References

1. W. R. Zipfel, R. M. Williams, and W. W. Webb, "Nonlinear magic: multiphoton microscopy in the biosciences," *Nat. Biotechnol.* **21**(11), 1369–1377 (2003).
2. E. E. Hoover and J. A. Squier, "Advances in multiphoton microscopy technology," *Nat. Photonics* **7**(2), 93–101 (2013).
3. D. Bird and M. Gu, "Compact two-photon fluorescence microscope based on a single-mode fiber coupler," *Opt. Lett.* **27**(12), 1031–1033 (2002).
4. M. T. Myaing, D. J. MacDonald, and X. Li, "Fiber-optic scanning two-photon fluorescence endoscope," *Opt. Lett.* **31**(8), 1076–1078 (2006).

5. D. R. Rivera et al., "Compact and flexible raster scanning multiphoton endoscope capable of imaging unstained tissue," *Proc. Natl. Acad. Sci. U.S.A.* **108**(43), 17598–17603 (2011).

6. W. Göbel et al., "Miniaturized two-photon microscope based on a flexible coherent fiber bundle and a gradient-index lens objective," *Opt. Lett.* **29**(21), 2521–2523 (2004).

7. S. Moon, G. Liu, and Z. Chen, "Multiphoton endoscopy based on a mode-filtered single-mode fiber," *Proc. SPIE* **7903**, 79032P (2011).

8. M. T. Myaing et al., "Enhanced two-photon biosensing with double-clad photonic crystal fibers," *Opt. Lett.* **28**(14), 1224–1226 (2003).

9. L. Fu, X. Gan, and M. Gu, "Nonlinear optical microscopy based on double-clad photonic crystal fibers," *Opt. Express* **13**(14), 5528–5534 (2005).

10. B. A. Flusberg et al., "*In vivo* brain imaging using a portable 3.9 gram two-photon fluorescence microendoscope," *Opt. Lett.* **30**(17), 2272–2274 (2005).

11. C. J. Engelbrecht et al., "Ultra-compact fiber-optic two-photon microscope for functional fluorescence imaging *in vivo*," *Opt. Express* **16**(8), 5556–5564 (2008).

12. S. Brustlein et al., "Double-clad hollow core photonic crystal fiber for coherent Raman endoscope," *Opt. Express* **19**(13), 12562–12568 (2011).

13. D. M. Huland et al., "Three-photon excited fluorescence imaging of unstained tissue using a GRIN lens endoscope," *Biomed. Opt. Express* **4**(5), 652–658 (2013).

14. K. Murari et al., "Compensation-free, all-fiber-optic, two-photon endomicroscopy at 1.55 μm," *Opt. Lett.* **36**(7), 1299–1301 (2011).

15. G. Liu et al., "Multiphoton microscopy system with a compact fiber-based femtosecond-pulse laser and handheld probe," *J. Biophotonics* **4**(1–2), 34–39 (2011).

16. M. Lelek et al., "Coherent femtosecond pulse shaping for the optimization of a non-linear micro-endoscope," *Opt. Express* **15**(16), 10154–10162 (2007).

17. C. Lefort et al., "Pulse compression and fiber delivery of 45 fs Fourier transform limited pulses at 830 nm," *Opt. Lett.* **36**(2), 292–294 (2011).

18. J. P. Gordon, "Theory of the soliton self-frequency shift," *Opt. Lett.* **11**(10), 662–664 (1986).

19. X.-H. Fang et al., "An all-photonic-crystal-fiber wavelength-tunable source of high-energy sub-100 fs pulses," *Opt. Commun.* **289**, 123–126 (2013).

20. G. McConnell and E. Riis, "Photonic crystal fibre enables short-wavelength two-photon laser scanning fluorescence microscopy with fura-2," *Phys. Med. Biol.* **49**(20), 4757–4763 (2004).

21. E. R. Andresen, P. Berto, and H. Rigneault, "Stimulated Raman scattering microscopy by spectral focusing and fiber-generated soliton as Stokes pulse," *Opt. Lett.* **36**(13), 2387–2389 (2011).

22. K. Wang and C. Xu, "Tunable high-energy soliton pulse generation from a large-mode-area fiber and its application to third harmonic generation microscopy," *Appl. Phys. Lett.* **99**(7), 071112 (2011).

23. D. G. Ouzounov et al., "Generation of megawatt optical solitons in hollow-core photonic band-gap fibers," *Science* **301**(5640), 1702–1704 (2003).

24. M. E. Pedersen et al., "Higher-order-mode fiber optimized for energetic soliton propagation," *Opt. Lett.* **37**(16), 3459–3461 (2012).

25. G. P. Agrawal, *Nonlinear Fiber Optics*, Academic Press, London, UK (2001).

26. A. Bétourné et al., "Control of supercontinuum generation and soliton self-frequency shift in solid-core photonic bandgap fibers," *Opt. Lett.* **34**(20), 3083–3085 (2009).

27. A. Bendahmane et al., "Solid-core photonic bandgap fiber for the generation of tunable high-energy solitons," in *3rd Workshop on Specialty Optical Fibers and Their Applications*, W3.36, Optical Society of America, Washington DC (2013).

28. O. Vanvincq et al., "Extreme deceleration of the soliton self-frequency shift by the third-order dispersion in solid-core photonic bandgap fibers," *J. Opt. Soc. Am. B* **27**(11), 2328–2335 (2010).

29. M. A. Albota, C. Xu, and W. W. Webb, "Two-photon fluorescence excitation cross sections of biomolecular probes from 690 to 960 nm," *Appl. Opt.* **37**(31), 7352–7356 (1998).

30. N. S. Makarov, M. Drobizhev, and A. Rebane, "Two-photon absorption standards in the 550–1600 nm excitation wavelength range," *Opt. Express* **16**(6), 4029–4047 (2008).

31. N. Ji, J. C. Magee, and E. Betzig, "High-speed, low-photodamage nonlinear imaging using passive pulse splitters," *Nat. Methods* **5**(2), 197–202 (2008).

Biographies of the authors are not available.